Imperial College London

Investigation on CTH Detector Response using Simulation Software

Author

CID: 01863260

Supervised by

Prof. Yoshi Uchida

Dr Yuki Fujii

Assessor

Dr Charles Naseby

Word Count

5228 words

A thesis submitted in fulfillment of requirements for the degree of
Bachelor of Science in Physics with Theoretical Physics

Department of Physics
Imperial College London

2024

Abstract

Cylindrical Trigger Hodoscope (CTH) detectors are designed for the COherent Muon to Electron Transition (COMET) experiment, which aims to detect neutrinoless muon-to-electron ($\mu - e$) transitions, a Beyond Standard Model (BSM) effect that requires detection devices with high accuracy to unveil. In order to examine the effectiveness of the CTH detectors, their responses upon encountering e^-, μ^+, and π^+ particles with initial momentum conditions of 105, 125, 150, and 200 MeV/c are collected using simulation software. The energy deposition behaviours are therefore compared with the theoretical predictions of the Bethe-Bloch formula, an expression describing the energy deposition per unit length as particles travel through materials. Evidently, in the COMET project's momentum range of interest at 105 MeV/c, e^- can be well distinguished from μ^+ and π^+ because of their distinct energy deposition behaviours, making the CTH detector an effective device to fulfil the COMET project's needs. Despite discrepancies, the general trend of energy deposition distribution from the simulation aligns with the Bethe-Bloch formula. The discrepancies are potentially resulted from secondary particle emissions or other radiative behaviours, which require further investigation.

Acknowledgments

Thanks to Dr Yuki Fujii for his invaluable guidance and instructions.

Thanks to Prof. Yoshi Uchida for his pivotal role in facilitating the realisation of this project.

Thanks to Dr Kou Oishi, Dr Per Josson, and Mr Roden Derveni, as well as other members of the Imperial College COMET group, for their unwavering support and dedication.

Furthermore, thanks to all other collaborators of the COMET project, whose preceding contributions have laid a robust groundwork for this BSc project.

Contents

1

Introduction

Contents

1.1 COMET Project

The COherent Muon to Electron Transition (COMET) project aims to search for neutrinoless conversion of muons into electrons ($\mu - e$ conversion) $\mu^- N \rightarrow e^- N$ for a given nucleus N. This is one of the charged-lepton flavour violation (CLFV) reactions [1]. Such processes are extremely suppressed in the Standard Model, with a branching ratio of $O(10^{-54})$ amidst the decay in orbit (DIO) process of $\mu^- \rightarrow e^- \nu_\mu \overline{\nu}_e$, which makes the $\mu - e$ conversion undetectable [2]. However, in some Beyond Standard Model (BSM) theories, such as Supersymmetry theories and the Leptoquark model, $\mu - e$ conversion is predicted with a branching ratio of $O(10^{-15})$.

The COMET project therefore aims to achieve a single-event sensitivity of 10^{-15} in its Phase-I to enable the detection of $\mu - e$ conversion, thereby confirming new physics beyond the Standard Model. This sensitivity will be further improved to 10^{-17} in Phase-II to enhance the study of CLFV [2].

1.2 CTH Detectors

The Cylindrical Detector (CyDet) is proposed as the primary detection device for COMET Phase-I. It comprises two main components: the Cylindrical Drift Chamber (CDC) and the Cylindrical Trigger Hodoscope (CTH), as depicted in Fig. 1.1.

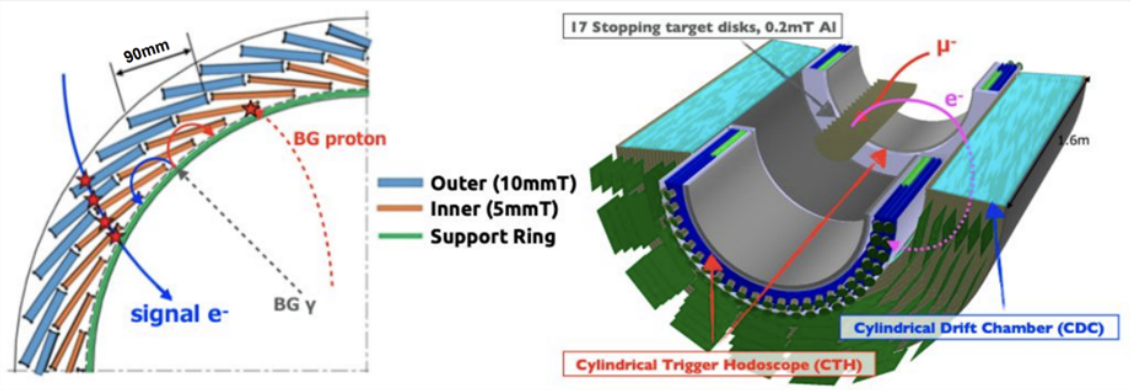

Figure 1.1: Left-hand side: illustration of the Cylindrical Trigger Hodoscope (CTH) detector. Right-hand side: the Cylindrical Detector (CyDet). The CTH detector is one of the two components of CyDet, providing accurate impact timing detection [3].

CDC is a gaseous chamber that allows accurate momentum detection of the charged particles. The incoming charged particles ionise the atomic e^- of the gas molecules upon impact, enabling them to drift under the strong electric field inside the chamber and collide with the detection wiring that records the momentum information. However, this drift leads to low timing resolution, complicating trajectory reconstruction of the charged particles.

To address this issue, the CTH detectors are proposed to be installed at both ends of the CDC to enable precise timing measurements. This setup allows charged particles generated at the centre of the CyDet to initially pass through the CDC, where their momentum readings are recorded. Subsequently, these particles traverse a strong magnetic field (1T) within the CyDet that bends their trajectories, leading them towards the CTH detectors where their timing information will be collected.

A CTH detector consists of two layers of concentric rings that contain 64 pairs of of inner (5 x 80 x 360 mm) and outer (10 x 88 x 340 mm) scintillators [2]. This structure allows the implementation of a 4-fold coincidence trigger algorithm to prevent false triggers from backgrounds, enabling the observation of the desired signals at a refined clarity.

1.3 Aim of The Project

This Bachelor of Science (BSc) project aims to better understand the response of CTH detectors upon encoutering various incidence radiations. Using simulation software, different signal information of the detectors are collected, including impact location, momentum and energy deposition distributions, as they encounter different particle types (e^-, μ^+, and π^+) under various initial momentum conditions (105, 125, 150 and 200 MeV/c). The collected information is therefore statistically analysed and compared against theoretical predictions. This helps determine the effectiveness of CTH detectors in fulfilling the COMET project's needs, and aids in future COMET Phase-I data analysis.

2

Theory

Contents

2.1 Energy Loss of a Charged Particle

As charged particles pass through matter, there are two primary processes [4]:

1) Inelastic collisions with the atomic electrons;

2) Elastic scattering with the nuclei.

The inelastic collisions are primarily responsible for the energy loss of the charged particles in matter. Upon impact, atomic electrons either enter an excited state or are ionised into substantial secondary particles (often referred to as delta-rays). In either scenario, energy is dissipated to the surrounding atoms, leading to energy deposition inside the material. Although the amount of energy transferred in each collision is small, the cumulative energy loss becomes observable due to the large number of collisions per unit length.

In contrast, elastic scattering deviates the charged particles from their original path without energy transfer.

Besides the two dominant processes, other processes include:

3) Emission of Cherenkov radiation;

4) Nuclear reactions;

5) Bremsstrahlung radiation.

These processes are extremely rare compared to atomic collision processes and are often omitted when analysing the energy loss of charged particles. Therefore, these processes will not be considered in this report.

2.2 The Bethe-Bloch Formula

The Bethe-Bloch formula is crucial in predicting the energy deposition behaviour of charged particles. It is named after Hans Bethe and Felix Bloch, who independently developed the formula and published their results in 1930. The formula is typically represented as [4]

$$-\frac{dE}{dx} = 2\pi N_a r_e^2 m_e c^2 \rho \frac{Z}{A} \frac{z^2}{\beta^2} \left[\ln\left(\frac{2m_e \gamma^2 v^2 W_{max}}{I^2} \right) - 2\beta^2 \right]. \tag{2.1}$$

The quantity dE/dx is typically referred to as the *stopping power*, which describes the energy lost per unit distance travelled inside the material.

The terms within the Bethe-Bloch formula can be categorised into three types: constants, material-dependent parameters, and particle-dependent parameters, which are detailed below.

2.2.1 Constants

1) N_a: Avogadro's number $= 6.022 \times 10^{23}\,\mathrm{mol}^{-1}$.

2) r_e: classical electron radius $= 2.817 \times 10^{-13}\,\mathrm{cm}$.

3) m_e: electron mass $= 9.11 \times 10^{-13}\,\mathrm{kg}$.

4) c: speed of light $= 3 \times 10^{8}\,\mathrm{m \cdot s^{-1}}$.

2.2.2 Material-Dependent Parameters

1) ρ: density of absorbing material.

2) Z: atomic number of absorbing material.

3) A: atomic weight of absorbing material.

4) I: mean excitation potential, which is related to Z as

$\frac{I}{Z} = 12 + \frac{7}{Z}\,\text{eV} \qquad Z < 13,$

$\frac{I}{Z} = 9.76 + 58.8\,Z^{-1.19}\,\text{eV} \qquad Z \geq 13.$

2.2.3 Particle-Dependent Parameters

1) z: charge of incident particle in units of e.

2) v: speed of incident particle.

4) γ: Lorentz factor $= 1/\sqrt{1-\beta^2}$, where $\beta = v/c$.

5) W_{max}: maximum energy transfer in a single collision.

For an incident particle of mass M,

$W_{max} = \frac{2m_e c^2 \eta^2}{1+2s\sqrt{1+\eta^2}+s^2}$,

where $s = m_e/M$ and $\eta = \beta\gamma$.

2.3 Length Contraction

Special relativity states that objects moving at high speeds relative to an observer's rest frame undergo contraction in the direction of their motion. This phenomenon is expressed as

$$L = \gamma L_0, \tag{2.2}$$

where L is the length of the moving object observed by a stationary observer, L_0 is the proper length of the object, and $\gamma = \sqrt{1 - \frac{v^2}{c^2}}$ is the Lorentz factor.

In the rest frame of a particle, the detector moves at high speed and thus appears shorter to the particle. This contraction effectively reduces the probability of interactions per unit length in the lab frame.

3

Methodology

Contents

3.1 Monte Carlo Simulation

Monte Carlo simulation uses a probabilistic model that simulates the outcomes of an experiment with repeated random sampling. It is commonly utilised in High Energy Physics to gather information on the experimental setup and detector performance before the experiment begins operation.

The data utilised in this project are obtained through Geant4-based simulation software, which employs Monte Carlo methods to simulate the behaviour of particles as they traverse through matter. Geant4 accounts for various physical processes such as electromagnetic interaction and particle decay. It also provides a flexible and powerful framework for defining complex geometries of experimental setups and materials [5].

The simulation software's geometry mirrors the setup of CTH prototype testing at the Paul Scherrer Institute conducted in November 2023, as depicted in Fig. 3.1. The layout comprises two outer scintillators - CTH counters 0 and 1, each 10 mm thick; and two inner scintillators -

CTH counters 2 and 3, each 5 mm thick. Additionally, four beamline counters are placed along the axis of the beam direction for validation purposes, with sizes of $10 \times 10\,\mathrm{mm}^2$, $10 \times 10\,\mathrm{mm}^2$, $200 \times 200\,\mathrm{mm}^2$ and $300 \times 300\,\mathrm{mm}^2$ respectively. The beam of charged particles is simulated from the left of the diagrams and passes through CTH counters 0, 1, 2, and 3 along the z-axis.

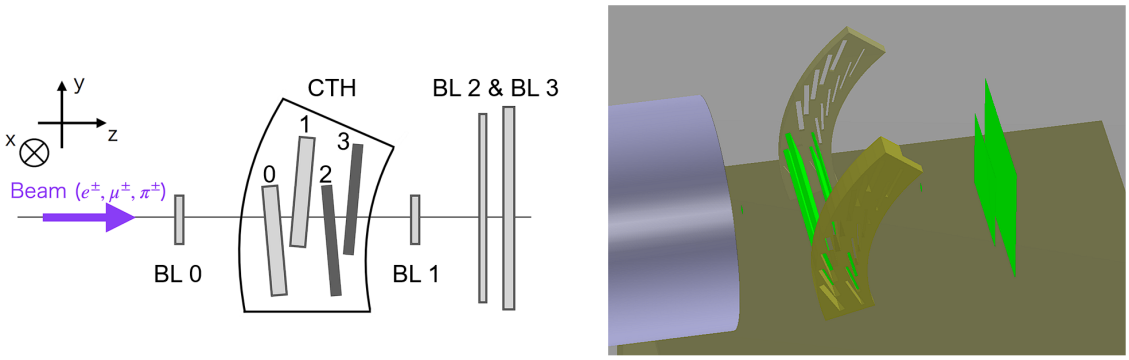

Figure 3.1: Left-hand side: schematic diagram of the CTH detector prototype testing at the Paul Scherrer Institute [6], whose setup comprises of 4 CTH counters and 4 Beamline (BL) counters. Right-hand side: simulation geometry in Geant4 software, which aligns with the setup of the CTH prototype testing.

By aligning the simulation geometry with the actual experimental setup, the information collected from Geant4 can be readily compared with the real data. Although the comparison analysis was not performed in this project, it will be a main focus hereafter.

In this project, simulations are performed with e^-, μ^+, and π^+ at momenta of 105 MeV/c, 125 MeV/c, 150 MeV/c and 200 MeV/c respectively. Each simulation contains 50,000 events to minimise statistical fluctuations. One simulation takes approximately 800 seconds using the Linux machine of the High Energy Physics (HEP) group of Imperial College.

3.2 Fitting Models

Function fitting is necessary to extract data statistically. To streamline the analysis, two models are focused on: the Landau distribution [7] and the Moyal distribution [8].

3.2.1 Landau Distribution

The Landau distribution is named after the physicist Lev Landau. It primarily describes the distribution of energy deposition of a charged particle inside thin materials. The formula is expressed as [7]

$$p(x;\mu,c) = \frac{1}{\pi c}\int_0^\infty e^{-t}\cos\left[t\left(\frac{x-\mu}{c}\right)+\frac{2t}{\pi}\log\left(\frac{t}{c}\right)\right]\,dt, \tag{3.1}$$

which is characterised by the location parameter μ and shape parameter c that determine the position and width of the distribution respectively.

This expression can be illustrated in Fig. 3.2, where the characteristic parameters are taken as $\mu = 0$ and $c = 1$ respectively. It is a continuous probability distribution with a heavy tail, allowing extreme energy deposition events to occur.

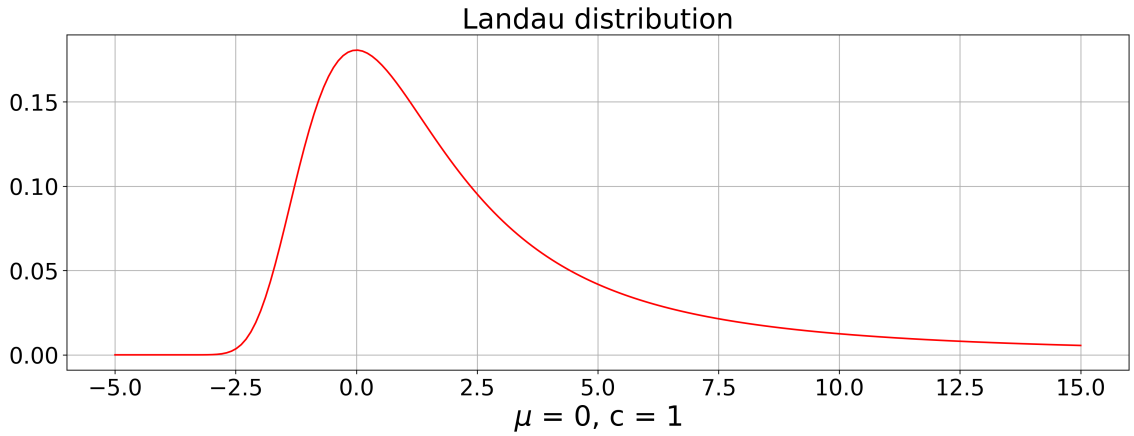

Figure 3.2: The Landau distribution with $\mu = 0$ and $c = 1$, which exhibits a positively skewed shape with heavy-tail behavior.

3.2.2 Moyal Distribution

The Moyal distribution is named after the mathematician José Enrique Moyal. It arises from the study of the convolution of two independent and random Gaussian variables, which often represent the position and momentum of a quantum particle. It is commonly applied to model the distributions of energy loss in particle physics experiments. The probability density function is written as [8]

$$p(\lambda,\sigma) = \frac{1}{\sqrt{2\pi}\sigma}\exp\left(-\frac{\lambda+e^{-\lambda}}{2}\right) \quad \text{where} \quad \lambda(x;\mu,\sigma) = \frac{x-\mu}{\sigma}. \tag{3.2}$$

An illustration of the Moyal distribution is shown in Fig. 3.3, where characteristic distributions are taken as $\mu = 0$ and $\sigma = 1$. Its shape is characterised by a peak slightly offset from its mean and a heavier tail compared to a normal distribution.

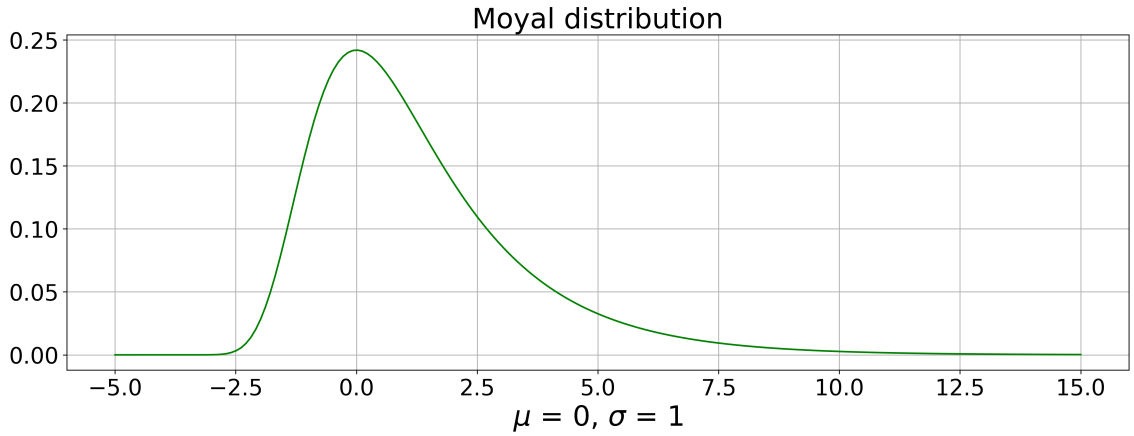

Figure 3.3: The Moyal distribution with $\mu = 0$ and $\sigma = 1$, which has a similar shape to the Landau distribution with a weaker tail behaviour.

3.2.3 Correlation Between Landau and Moyal

The Landau distribution with $\mu = 0$ and $c = 1$ and the Moyal distribution with $\mu = 0$ and $\sigma = 1$ are plotted in Fig. 3.4.

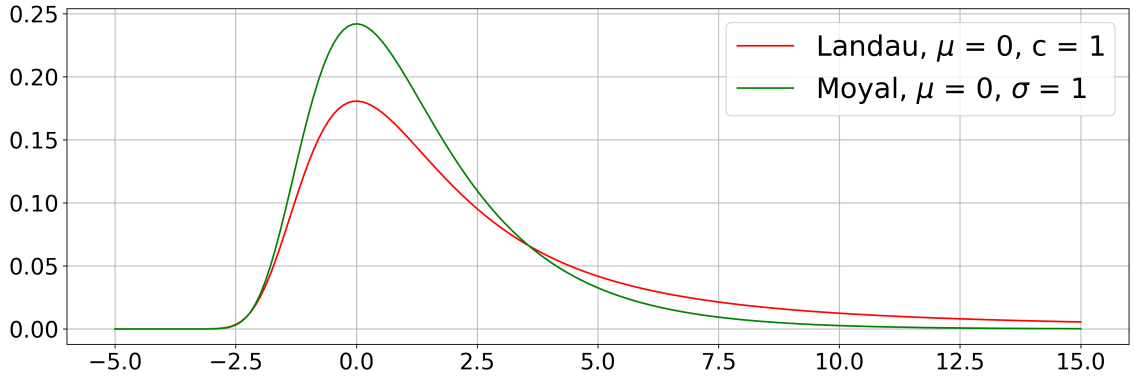

Figure 3.4: The Landau distribution ($\mu = 0$ and $c = 1$) and the Moyal distribution ($\mu = 0$ and $\sigma = 1$) exhibit similar general shapes. The Landau distribution demonstrates a stronger tail behaviour compared to the Moyal distribution.

Both shapes are positively skewed with a mode less than their mean. Compared to the Moyal distribution, Landau exhibits stronger tail behaviour.

As a matter of fact, the Moyal distribution is derived as an approximation of the Landau distribution under the limit of a large mean number of collisions $Q \geq 20$ [8]. Therefore, as the number of interactions between a particle and the detector increases, the distribution tends Moyal in nature.

3.3 Effective Atomic Number and Atomic Weight

As detailed in Section 2.2, four material-dependent parameters (ρ, Z, A and I) of the CTH detectors need to be substituted into the Bethe-Bloch formula. Among these, the material density $\rho = 1.032\,\mathrm{g}\cdot\mathrm{cm}^{-3}$ is provided by the scintillator manufacturer, and the mean excitation potential is known to be $I = 64.7\,\mathrm{eV}$ for plastic scintillators [4]. This leaves the atomic number Z and the atomic weight A of the scintillators to be determined.

The primary composition of scintillation detectors is Polyvinyl toluene (PVT) material, with a chemical formula of $[CH_2CH(C_6H_4CH_3)]n$ [9]. Through which, the effective atomic number (Z_{eff}) and effective atomic weight (A_{eff}) can be calculated using [10]

$$Z_{eff}^{2.94} = \sum_n f_n \times Z_n^{2.94}, \qquad A_{eff}^{2.94} = \sum_n w_n \times A_n^{2.94}, \tag{3.3}$$

where f_n represents the fraction of the total number of electrons and w_n represents the fraction of the total weight associated with each element n. This yields $Z_{\mathrm{eff}} = 5.665$ and $A_{\mathrm{eff}} = 11.653$. These values are reasonably close to those of carbon ($Z = 6$, $A = 12.011$), which is the primary component of PVT material, as expected.

With these parameters, the stopping power (dE/dx) against momentum (p) distribution can be plotted using Eq. 2.1 for e^-, μ^+ and π^+, as shown in Fig. 3.5. The masses of these particles are $m_e = 0.511\,\mathrm{MeV/c^2}$, $m_\mu = 105.7\,\mathrm{MeV/c^2}$, and $m_\pi = 139.6\,\mathrm{MeV/c^2}$ respectively. Heavier particles have distinctly larger stopping powers, especially at lower momenta.

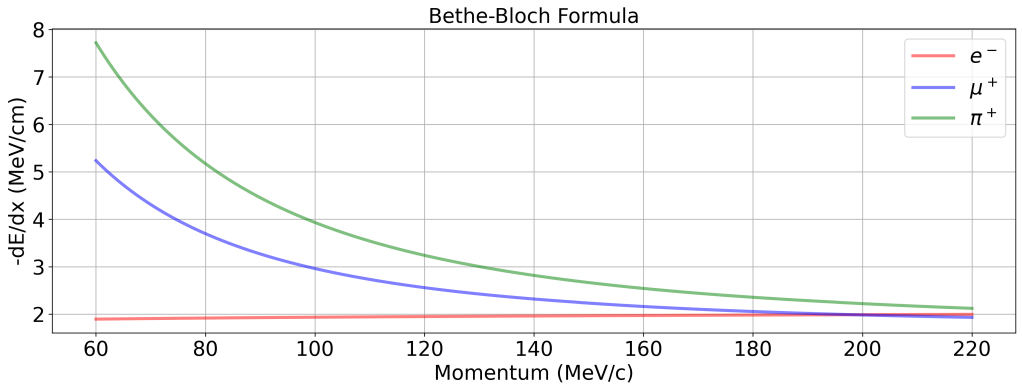

Figure 3.5: The Bethe-Bloch formula for PVT material plotted for e^-, μ^+, and π^+ particles, with masses $m_e = 0.511\,\mathrm{MeV/c^2}$, $m_\mu = 105.7\,\mathrm{MeV/c^2}$, and $m_\pi = 139.6\,\mathrm{MeV/c^2}$, respectively. At low momenta, heavier particles deposit more energy. As momentum increases, their stopping powers become closer.

This is potentially a consequence of relativistic effect. In fact, the velocity v of a particle with momentum p and mass m can be calculated using

$$v = \frac{pc}{\sqrt{c^2m^2 + p^2}}, \tag{3.4}$$

hence when particles have the same momentum, heavier particles typically exhibit lower velocities compared to lighter particles. Consequently, heavier particles have smaller values of β, resulting in larger values of $-dE/dx$ according to Eq. 2.1. This observation aligns with the trends depicted in Fig. 3.5, given that $m_\pi > m_\mu > m_e$.

4

Results

Contents

4.1 Impact Location Distribution

The impact location distributions, which represents the initial location of particles upon encountering each of the CTH counters, are extracted from the Monte Carlo simulation for e^-, μ^+ and π^+ with various initial momenta. A histogram illustrating the impact location distributions in the x and y directions for particles with an initial momentum of 105 MeV/c is displayed in Fig. 4.1.

The shape of the distributions in both the x and y directions for each of the counters are approximately Gaussian. This can be a consequence of the primary positions of the particles are sampled using Gaussian distributions with $\mu = 0$ and $\sigma = 10$ in the simulation software. Additionally, particles experience random scattering as they traverse through the detectors. According to the central limit theorem (CLT), this also contributes to the Gaussian shape.

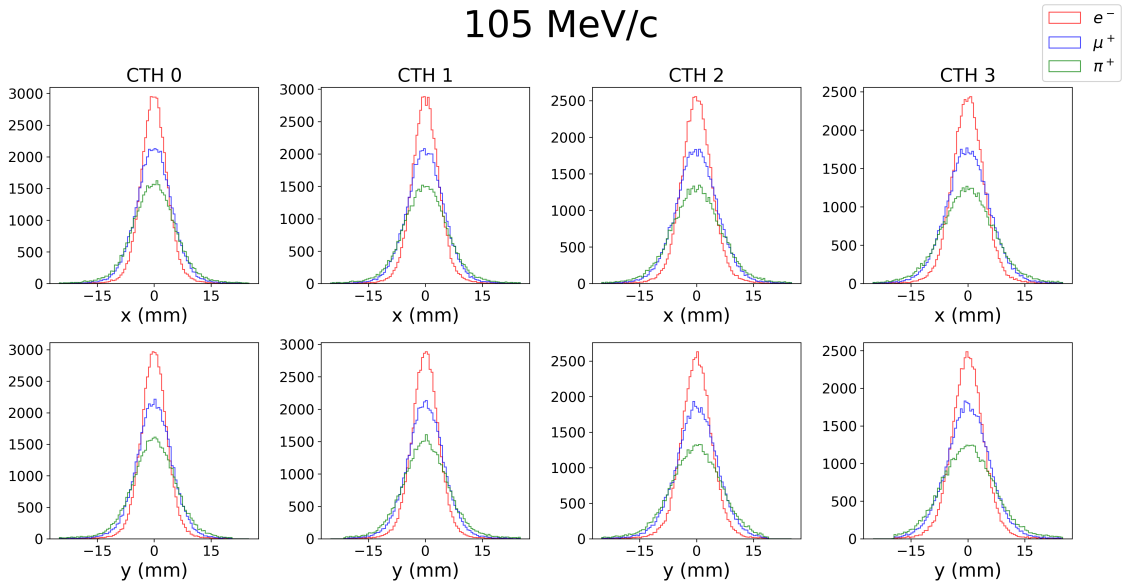

Figure 4.1: The impact location distributions of e^-, μ^+, and π^+ with an initial momentum of 105 MeV/c plotted as histograms of 200 bins, with the vertical axis being the frequency readings. All of the distributions are approximately Gaussian.

4.1.1 Scattering Analysis

Gaussian distributions are fitted to the impact location distributions, with the x distributions at CTH 0 from Fig. 4.1 serving as an example, as illustrated in Fig. 4.2.

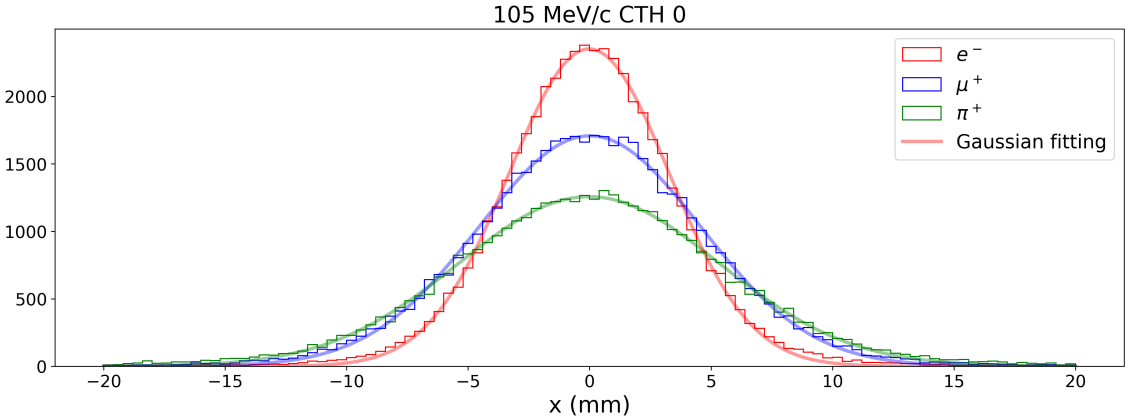

Figure 4.2: The Gaussian fitting of the x distribution at CTH 0 with an initial momentum of 105 MeV/c shows that all three particles are well-fitted by the Gaussian model.

Similar fitting procedures are applied to other distributions. A table displaying the sigma values of the fitted Gaussian distributions is presented in Table 4.1.

Given $m_\pi > m_\mu > m_e$, it is evident that heavier particles exhibit higher σ values in the Gaussian fitting. This indicates a wider spreading of the distribution, suggesting stronger scattering effects.

σ of Fitted Gaussian Distributions

		CTH 0	CTH 1	CTH 2	CTH 3
x	e^-	3.31(1)	3.43(2)	3.85(2)	4.03(2)
	μ^+	4.55(2)	4.74(2)	5.35(3)	5.60(3)
	π^+	5.37(3)	5.59(3)	6.34(4)	6.68(4)
y	e^-	3.29(1)	3.41(2)	3.84(2)	4.02(2)
	μ^+	4.50(2)	4.67(2)	5.26(3)	5.51(3)
	π^+	5.45(3)	5.68(4)	6.49(3)	6.83(4)

Table 4.1: The standard deviation of the fitted Gaussian distributions for x and y values of particles with initial momentum of 105 MeV/c. Numbers in the brackets are the errors corresponding to the last digit of the readings. Heavier particles consistently exhibit higher σ values than the lighter ones.

Relativistic effect likely plays a role in this phenomenon. Although the particles start with similar momenta, according to Eq. 3.4, lighter particles have higher velocities that result in higher Lorentz factors γ, which induces stronger length contraction as per Eq. 2.2. Consequently, lighter particles perceive shorter distances when travelling through the material, leading to a decreased probability of electromagnetic interactions per unit length in the lab frame and thus less spread in the impact location distributions.

Comparing the impact location distributions of different initial momenta at CTH 3, as depicted in Fig. 4.3, it can be observed that as momentum increases, the distributions of μ^+ and π^+ tend towards the momentum distribution of e^-. This trend potentially arises as the particles become equally relativistic at high momenta.

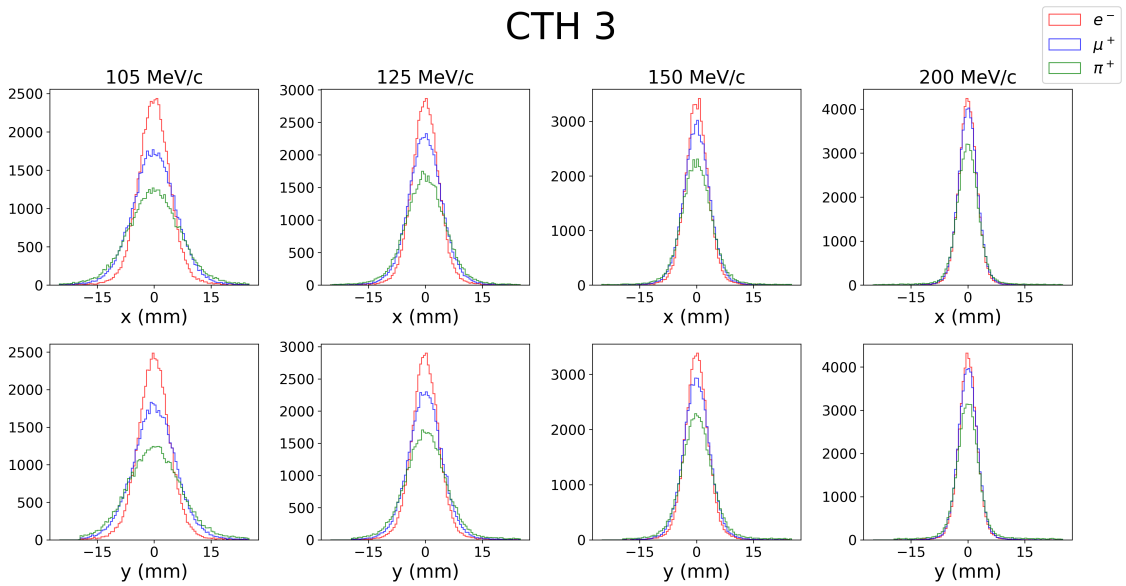

Figure 4.3: The x and y distributions at CTH 3 are shown for initial momenta of 105, 125, 150, and 200 MeV/c respectively. The shape remains Gaussian as momentum increases, and the distributions of μ^+ and π^+ approaches that of e^-.

4.2 Path Length Distribution

The path length is a measurement of the trajectory length that particles travel inside the counters. A histogram of the path lengths of e^-, μ^+, and π^+ with initial momenta of 105 MeV/c are plotted in Fig. 4.4.

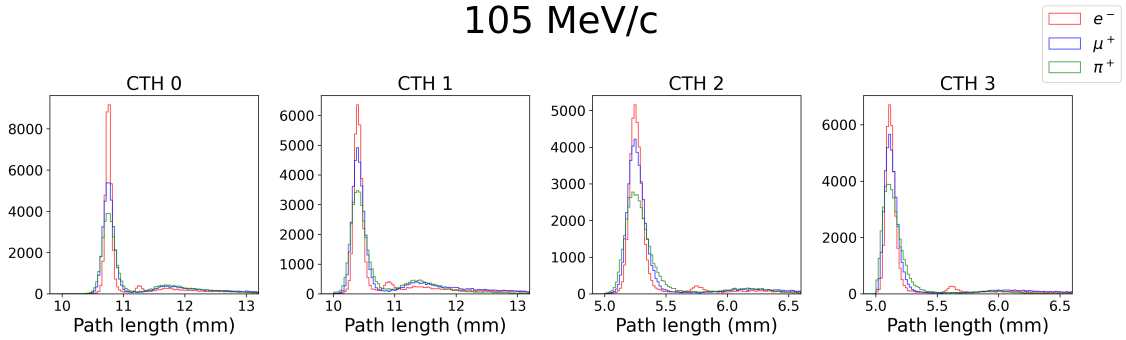

Figure 4.4: The path length distributions of particles with initial momenta of 105 MeV/c. CTH 0 and 1 have a thickness of 10 mm, CTH 2 and 3 have a thickness of 5 mm; the x-axis of each histogram is scaled accordingly. The distributions exhibit nearly Gaussian primary peaks followed by subsequent bumps.

Since CTH counters 0 and 1 have a thickness of 10 mm, counters 2 and 3 have a thickness of 5 mm, the ranges of the plots are scaled accordingly. Despite this difference, all four distributions exhibit similar shapes with a primary peak that is approximately Gaussian, followed by secondary bumps.

4.2.1 Expected Path Lengths

The expected path length can be calculated from the geometry of the detectors on the right-hand side of Fig. 3.1 using

$$\text{Expected Path Length} = \frac{\text{Counter Thickness}}{\cos\theta}, \tag{4.1}$$

where θ is the angle that the detector width makes with the z-axis, as shown in Fig. 4.5.

This yields the expected path lengths for each counter as follows: CTH 0: 10.748 mm; CTH 1: 10.403 mm; CTH 2: 5.257 mm; and CTH 3: 5.112 mm. These values can be plotted onto their corresponding distributions, as shown in Fig. 4.6. Each expected value aligns with the peak of its corresponding path length distribution, providing evidence of the valid analysis method.

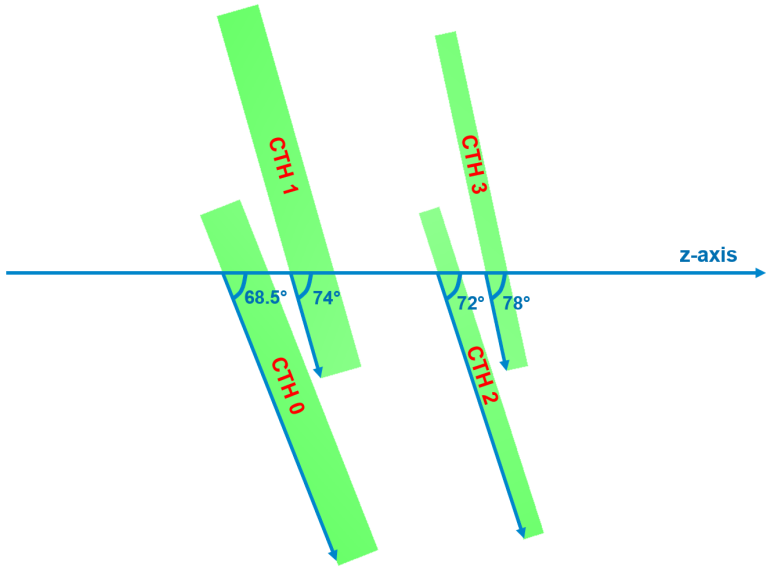

Figure 4.5: The CTH counters with their angles from the z-axis labelled as follows: CTH 0: 68.5°; CTH 1: 74°; CTH 2: 72°; and CTH 3: 78°. These angles can be utilised to compute the expected path length of each CTH counter.

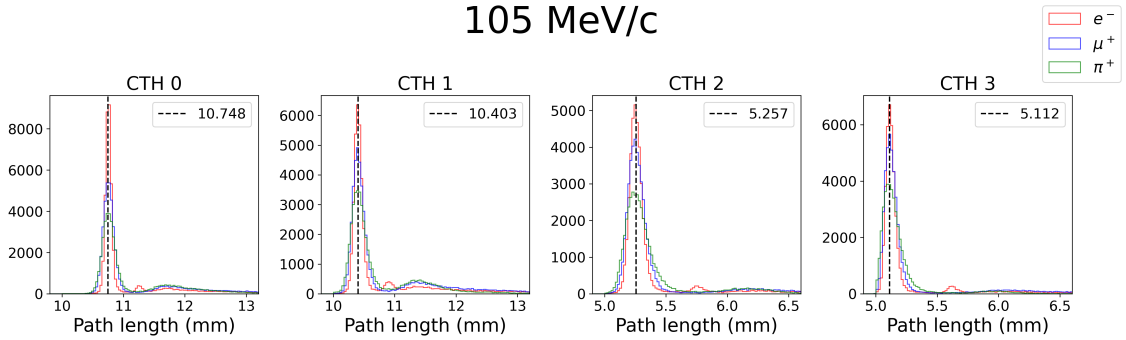

Figure 4.6: The path length distributions for particles with an initial momentum of 105 MeV/c are shown, along with the expected path lengths at CTH 0: 10.748 mm; CTH 1: 10.403 mm; CTH 2: 5.257 mm; and CTH 3: 5.112 mm. These values are aligned with the primary peak of the distributions.

4.2.2 Elastic Scattering Analysis

The path lengths at CTH 0 for different initial momenta are plotted in Fig. 4.7. As momentum increases, the distribution of path lengths becomes more concentrated around a single point.

By limiting the y-values to (0, 1000), the secondary peaks can be observed with better detail, as shown in Fig. 4.8. All three particles exhibit a secondary peak at a similar position, except e^- has an additional peak between the primary and secondary peaks. This additional peak is potentially a result of the detection of delta-ray trajectories, which are the ionised atomic electrons produced from hard collisions inside the detector.

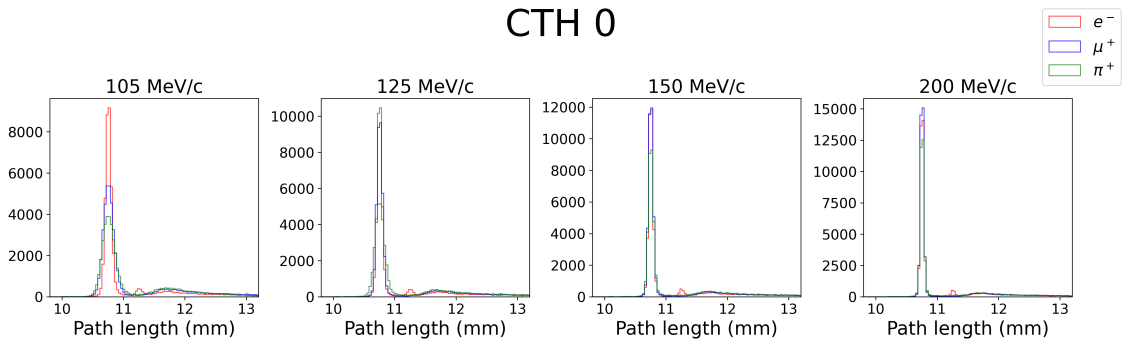

Figure 4.7: The path length distributions of CTH 0 with different initial momenta are depicted. As momentum increases, the primary peak becomes thinner, and the distributions of μ^+ and π^+ approach that of e^-.

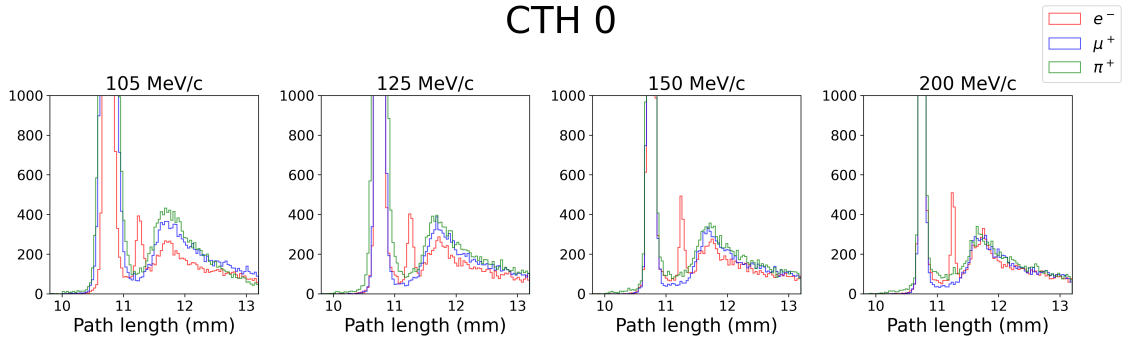

Figure 4.8: Path length distributions of CTH 0 with different initial momenta are presented, with y-values limited to (0, 1000). All three particles exhibit secondary peaks of similar shape at approximately the same location, with e^- showing an additional peak between the primary and secondary peaks.

The other secondary peaks, on the other hand, are potentially consequences of elastic scatterings, leading particles to scatter towards certain angles at higher probabilities. Similar to the primary peaks, secondary peaks merge into each other as momenta increase. Further investigation is in demand to enhance the comprehension of this behaviour.

4.3 Momentum and Stopping Power Distributions

The simulation software outputs information regarding the initial momentum p of particles upon encountering the counters, as well as the energy deposition ΔE. Dividing the energy deposition by the trajectory length returns the energy deposition per unit path length $\Delta E/\Delta x$, which is an approximation of the stopping power dE/dx.

The p and $\Delta E/\Delta x$ distributions for particles with initial momenta of 105 MeV/c are plotted in Fig. 4.9. The top row illustrates that heavier particles lose momentum at a greater rate. This

is a consequence of heavier particles losing more energy, which can be observed in the bottom row of the plot.

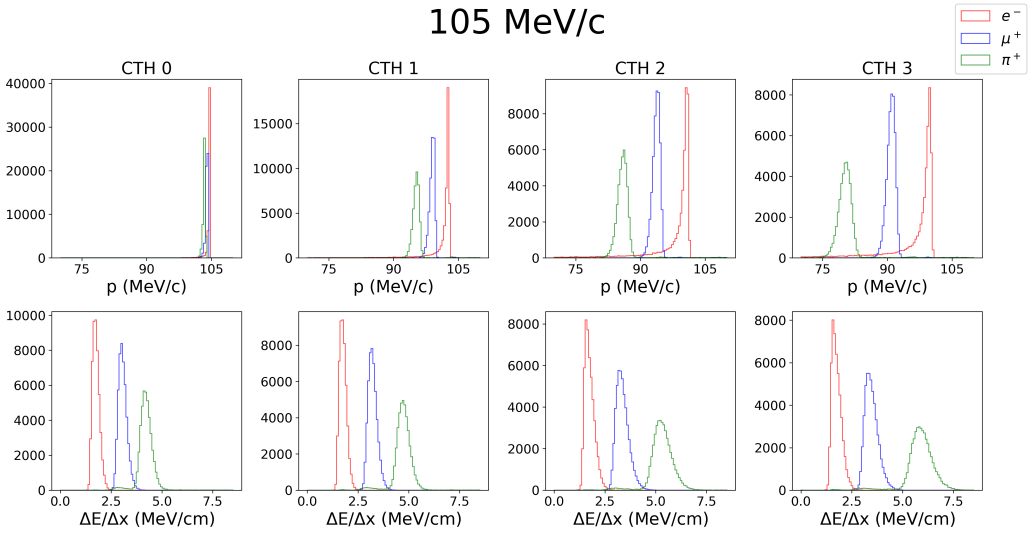

Figure 4.9: The p distributions (top) and $\Delta E/\Delta x$ distributions (bottom) of particles with initial momenta of 105 MeV/c. Heavier particles deposit more energy per unit length and lose momentum faster.

The increase in energy deposition of particles as they pass through detectors aligns with the expectation of relativistic effects. As particles lose momentum, they become less relativistic and experience less length contraction. This increases their probability of interacting with the detector, resulting in a higher energy deposition.

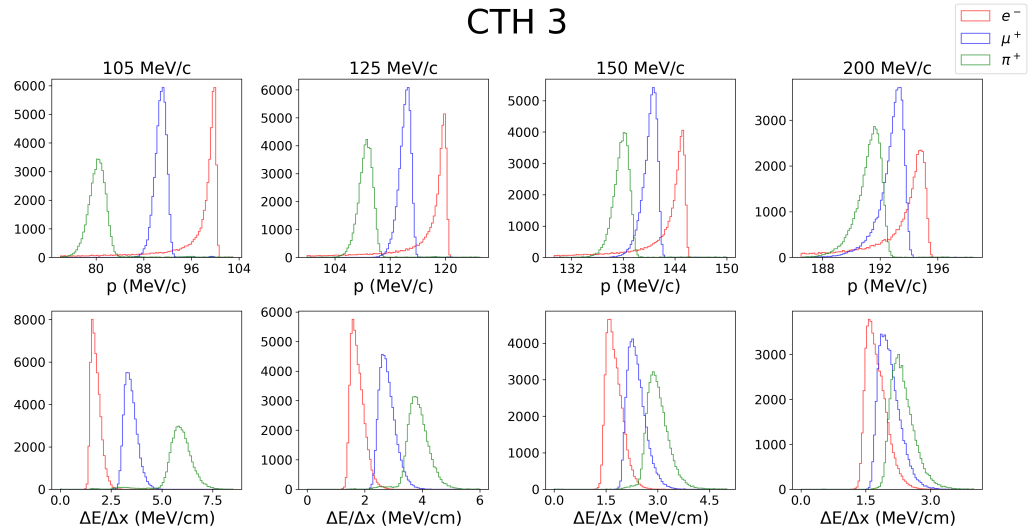

Figure 4.10: The distributions of p (top) and $\Delta E/\Delta x$ (bottom) at CTH 3 for different initial momenta. As momentum increases, the distributions of the three particles merge into each other, making them harder to distinguish under real experimental conditions.

The distributions of p and $\Delta E/\Delta x$ at CTH 3 for particles with different initial momenta are depicted in Fig. 4.10. As initial momenta increase, the distributions merge into each other and become increasingly difficult to distinguish. This observation aligns with our expectation from the Bethe-Bloch formula (Fig. 3.5), wherein as momenta increase, the three particles become equally relativistic and exhibit similar energy deposition behaviours, resulting in similar momentum distributions at each counter.

4.3.1 Fitting of Landau and Moyal Distributions

To analyse the data more quantitatively, Landau and Moyal distributions are fitted onto the p and $\Delta E/\Delta x$ readings. Despite being originally designed to describe energy deposition behaviours, due to the correlation between momentum and stopping power, Landau and Moyal distributions can be fitted to the p readings as well. An example of such fitting is shown in Fig. 4.11, where both Landau and Moyal distributions (flipped in horizontal direction) are fitted onto the p readings at CTH 3 for particles with initial momenta of 125 MeV/c.

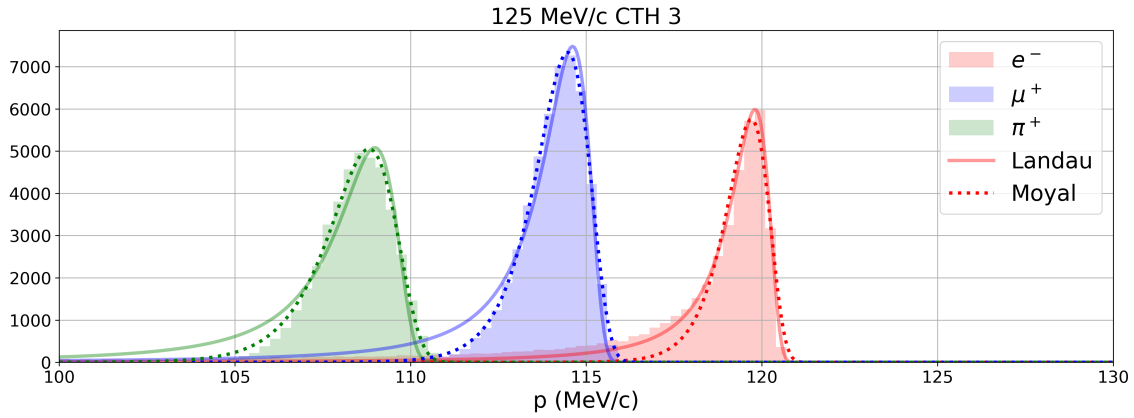

Figure 4.11: The p readings at CTH 3 fitted with Landau (solid lines) and Moyal (dotted lines) distributions for particles with initial momenta of 125 MeV/c. For e^-, the Landau distribution provides a better fit, whereas the Moyal distribution fits μ^+ and π^+ better.

As depicted in the graph, the Landau distribution better fits the momentum readings of e^-, while μ^+ and π^+ prefer the Moyal distribution. Therefore, p and $\Delta E/\Delta x$ readings of different particles of different initial momenta may favour different fitting distributions at different CTH counters.

To determine the better fitting distribution of each reading, chi-squared values of the Landau and Moyal distributions fitted onto each reading are compared using

$$\chi^2 = \sum \frac{(O_i - E_i)^2}{E_i}, \tag{4.2}$$

where O_i represents the observed bin and E_i denotes the expected value predicted by either the Landau or Moyal distribution at the corresponding bin. A lower chi-squared value indicates that the fitting distribution better describes the histogram.

For particles with an initial momentum of 105 MeV/c, the chi-squared values under the Landau and Moyal distributions are listed in Table 4.2. The chi-squared values of the two models are compared, with the lower value highlighted in either red (for Landau) or green (for Moyal). This allows for the determination of the better fit for each distribution.

105 MeV/c

		CTH 0			CTH 1		
		e^-	μ^+	π^+	e^-	μ^+	π^+
p	Landau	10.21	25.38	60.97	73.98	115.97	244.20
	Moyal	6174.02	1246.55	111.50	12686.20	9.58	19.89
	Better fit	Landau	Landau	Landau	Landau	Moyal	Moyal
$\frac{\Delta E}{\Delta x}$	Landau	198.60	280.23	969.75	184.58	703.45	324.91
	Moyal	51.79	51.95	108.12	64.70	60.79	133.19
	Better fit	Moyal	Moyal	Moyal	Moyal	Moyal	Moyal
		CTH 2			CTH 3		
		e^-	μ^+	π^+	e^-	μ^+	π^+
p	Landau	172.14	212.65	495.38	228.36	630.92	1394.66
	Moyal	12279.8	20.21	62.35	11130.80	35.85	128.90
	Better fit	Landau	Moyal	Moyal	Landau	Moyal	Moyal
$\frac{\Delta E}{\Delta x}$	Landau	100.15	191.06	674.48	100.33	191.01	543.17
	Moyal	35.05	10.15	56.33	35.31	12.47	44.43
	Better fit	Moyal	Moyal	Moyal	Moyal	Moyal	Moyal

Table 4.2: The chi-squared values of the p and $\Delta E/\Delta x$ readings for particles with an initial momentum of 105 MeV/c fitted by Landau and Moyal distributions are compared. This comparison helps determine the favoured model for each distribution.

Similar methods are applied for particles with other initial momenta. The favoured fitting distribution of p and $\Delta E/\Delta x$ readings are listed in Table 4.3.

Despite all p readings starting with Landau at CTH 0, those of heavier particles tend to transform into Moyal as they pass through subsequent detectors, especially at low momenta. As initial momentum increases, Landau distribution becomes harder to disrupt, persisting longer through several counters. This may result from the relativistic effect of higher momentum particles interacting less with the detector.

On the other hand, $\Delta E/\Delta x$ readings prefer Moyal for all particles across all four initial mo-

		105 MeV/c				125 MeV/c			
		CTH 0	CTH 1	CTH 2	CTH 3	CTH 0	CTH 1	CTH 2	CTH 3
p	e^-	Landau	Landau	Landau	Landau	Landau	Landau	Landau	Landau
	μ^+	Landau	Moyal	Moyal	Moyal	Landau	Moyal	Moyal	Moyal
	π^+	Landau	Moyal	Moyal	Moyal	Landau	Moyal	Moyal	Moyal
$\frac{\Delta E}{\Delta x}$	e^-	Moyal	Moyal	Moyal	Moyal	Moyal	Moyal	Moyal	Moyal
	μ^+	Moyal	Moyal	Moyal	Moyal	Moyal	Moyal	Moyal	Moyal
	π^+	Moyal	Moyal	Moyal	Moyal	Moyal	Moyal	Moyal	Moyal
		150 MeV/c				200 MeV/c			
		CTH 0	CTH 1	CTH 2	CTH 3	CTH 0	CTH 1	CTH 2	CTH 3
p	e^-	Landau	Landau	Landau	Landau	Landau	Landau	Landau	Landau
	μ^+	Landau	Landau	Moyal	Moyal	Landau	Landau	Landau	Landau
	π^+	Landau	Moyal	Moyal	Moyal	Landau	Landau	Moyal	Moyal
$\frac{\Delta E}{\Delta x}$	e^-	Moyal	Moyal	Moyal	Moyal	Moyal	Moyal	Moyal	Moyal
	μ^+	Moyal	Moyal	Moyal	Moyal	Moyal	Moyal	Moyal	Moyal
	π^+	Moyal	Moyal	Moyal	Moyal	Moyal	Moyal	Moyal	Moyal

Table 4.3: The favored fitting distributions of the p and $\Delta E/\Delta x$ readings for each initial momentum level are summarised. As momentum increases, the p readings tend to favour Landau, while the $\Delta E/\Delta x$ readings consistently favour Moyal.

menta. This preference could stem from particles interacting with the detector with a large mean number of collisions due to the relatively thick detectors (thickness of 5 or 10 mm). In such cases, Moyal distribution is favoured to describe the energy deposition, as mentioned in Section 3.2.

4.3.2 Fitted MPV Values and Bethe-Bloch Formula

By fitting the favoured model according to Table 4.3, the most probable values (MPV), which are the peak positions of the histograms, of the p and $\Delta E/\Delta x$ distributions can be obtained. Since all p readings of CTH counters represent the initial momentum value upon first encountering the particles, the average p inside each counter can be obtained by calculating the average of the MPV values of adjacent counters. For the average p of CTH 3, the MPV values at BL 2 (as shown in Fig. 3.1), which collects the p information after CTH 3, are requried. BL 2 covers a large area after CTH 3, enabling it to capture the vast majority of the signals.

The MPV values of p and $\Delta E/\Delta x$ readings for particles with an initial momentum of 105 MeV/c are listed in Table 4.4. The errors on the MPV values are obtained from Python's **scipy.optimize.curve_fit** algorithm, which yields very small uncertainties due to the large number of entries in each histogram (~50,000). Similar methods are applied for distributions of other initial momentum levels. These MPV values can hence be plotted onto the Bethe-Bloch formula, as shown in Fig. 4.12. Despite discrepancies, the general trend of the simulation results is well predicted by the Bethe-Bloch formula.

105 MeV/c					
		CTH 0	CTH 1	CTH 2	CTH 3
p	e^-	103.641(1)	101.758(5)	100.302(9)	99.26(1)
	μ^+	101.629(3)	96.594(5)	92.604(7)	89.67(1)
	π^+	99.496(5)	90.84(1)	83.42(2)	77.27(3)
$\frac{\Delta E}{\Delta x}$	e^-	1.687(1)	1.692(2)	1.636(3)	1.638(3)
	μ^+	2.989(1)	3.141(2)	3.234(1)	3.337(1)
	π^+	4.141(3)	4.658(3)	5.195(3)	5.789(5)

Table 4.4: MPV values of p and $\Delta E/\Delta x$ for particles with initial momenta of 105 MeV/c obtained from Landau / Moyal fitting. The errors are small due to low statistical uncertainties.

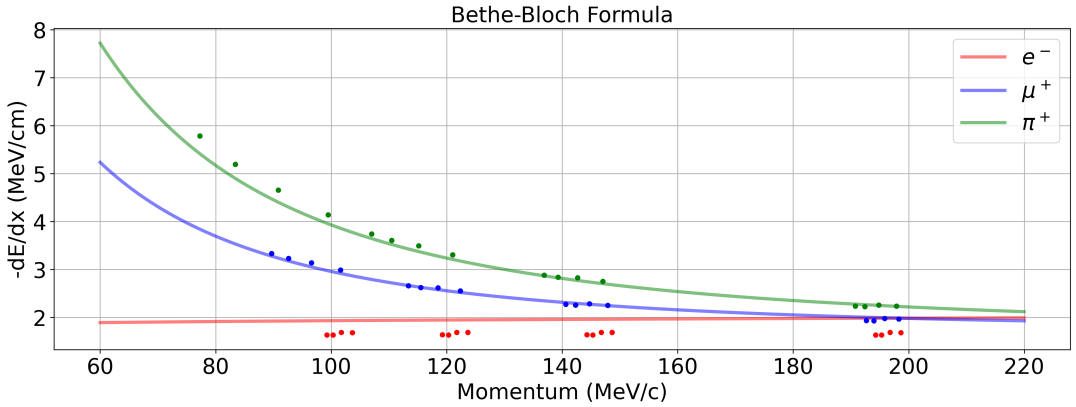

Figure 4.12: The fitted values are plotted onto the Bethe-Bloch formula. However, the errors are too small to be visible. Notable observations include a constant offset for e^- and misalignment for π^+ at low momenta.

The relative differences of the fitted values from the Bethe-Bloch formula can be analysed, for example, at CTH 0 and at CTH 3, as shown in Fig. 4.13 and Fig. 4.14. From left to right, the particles have initial momenta of 105, 125, 150, and 200 MeV/c respectively. Uncertainties associated with every point are magnified by a factor of 100.

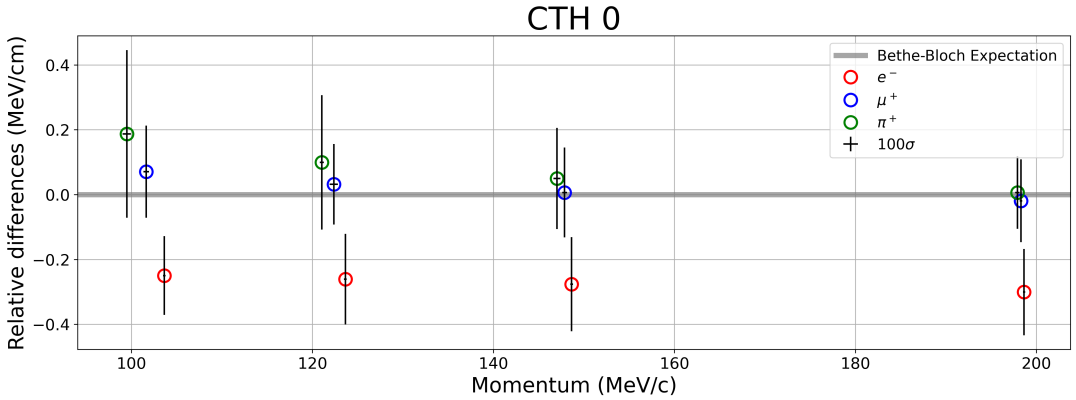

Figure 4.13: The relative differences of CTH 0 readings from the Bethe-Bloch predictions. From left to right, the particles have initial momenta of 105, 125, 150, and 200 MeV/c respectively. e^- exhibits an offset of about -0.3 MeV/cm, and π^+ misaligns at low momenta.

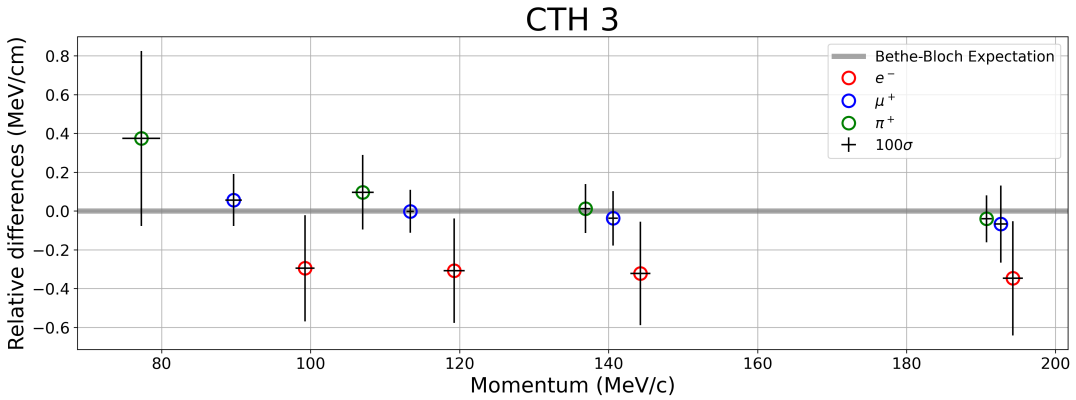

Figure 4.14: The relative differences of CTH 3 readings from the Bethe-Bloch predictions. From left to right, the particles have initial momenta of 105, 125, 150, and 200 MeV/c respectively. Compared to the CTH 0 readings (Fig. 4.13), the p readings of different particles separate further at lower momenta.

Particles within the same initial momentum groups exhibit similar momentum at CTH 0. As they pass through subsequent counters, the momentum readings separate significantly when they arrive at CTH 3. The separation becomes more pronounced as the initial momentum decreases, which aligns with our observation in Fig. 4.10.

There are offsets for e^- across all momentum levels, where each point is about 0.3 MeV/cm below the Bethe-Bloch prediction. This discrepancy could be due to the inclusion of the delta-ray path lengths into the path lengths of the primary particle, effectively increasing the overall e^- path length readings and hence decreasing $\Delta E/\Delta x$ values.

Misalignments for π^+ at low momenta may arise from the decay process of $\pi^+ \to \mu^+ + \nu_\mu$ with a mean lifetime of 26 ns. Using Eq. 3.4, π^+ at 105 MeV/c is found to travel at $1.8 \times 10^7\,\mathrm{m \cdot s^{-1}}$, which requires approximately 2 ns to travel through the entire detector. This is comparable to the π^+ mean lifetime, therefore π^+ is possible to decay when travelling through the counters, effectively transforming it into μ^+ with a lower momentum, which potentially deposits more energy than the original π^+ according to the Bethe-Bloch formula (Fig. 3.5), leading to a rise in the corresponding $\Delta E/\Delta x$ values. As momentum increases, the relativistic effect reduces the likelihood of π^+ decay before it reaches to the end of the detectors, leading to a better alignment with the prediction.

μ^+, on the other hand, has a longer mean lifetime of 2.2 µs, hence has a small likelihood of decay as it travels through the CTH counters, aligning the energy deposition distributions better with the Bethe-Bloch predictions.

5 Discussion

Contents

5.1 Impact Location

The impact locations are generally Gaussian for all initial momenta of e^-, μ^+, and π^+. This is likely due to:

1) The primary locations of particles being generated with a Gaussian distribution of $\sigma = 10$ mm;

2) The random scattering process leading to normally distributed impact locations.

For less relativistic particles, such as heavier particles with lower momentum, the Gaussian distributions have a larger σ. This is potentially a consequence of less relativistic particles interacting more frequently with the detector, resulting in a more evenly spread Gaussian distribution.

As the initial momenta of e^-, μ^+, and π^+ increase, their impact location distributions merge into each other, likely due to the particles approaching similar levels of relativistic speed.

5.2 Path Length

Each path length distribution of e^-, μ^+, and π^+ exhibits a primary peak centred around the expected path length that is calculated based on the thickness and orientation of each counter.

Additionally, all three particles display a secondary peak at a similar location. This secondary peak may be attributed to elastic scattering. e^- also manifests another peak situated between the primary and secondary peaks. This peculiar feature could arise from the inclusion of delta-rays in the path length of primary e^-. Further investigation is required to elucidate this secondary particle behaviour.

5.3 Energy Deposition

Less relativistic particles tend to deposit more energy per unit length as they travel through the detector material, primarily due to their increased interaction with atomic electrons, which undergo inelastic collisions responsible for energy loss.

As momentum increases, e^-, μ^+, and π^+ exhibit similar distributions for energy deposition as the particles approach relativistic equivalence.

The Moyal distribution fits well for the $\Delta E/\Delta x$ distributions, likely due to the relatively thick detectors that cause particles to undergo sufficient collisions with a mean number of collisions $Q > 20$, thus favouring the Moyal distribution over the Landau distribution.

A more universal fitting method can potentially be deployed to compare different histograms parallelly.

5.4 Momentum

As particles travel through detectors, momentum decreases due to energy deposition. Less relativistic particles experience greater momentum loss due to their higher stopping power.

Although Moyal and Landau distributions are commonly used to describe energy deposition, the correlation between energy deposition and momentum allows the latter to also be represented by a flipped Moyal or Landau distribution.

For all three particles at all initial momentum levels, momentum distributions start as Landau at CTH 0. This is potentially a consequence of the generated incidence particles pass through the thin BL 0 before arriving at CTH 0, which coincides with the situation (thin detector) that is specifically described by Landau distribution, whereas Moyal describes the thicker detector circumstances.

As particles progress through the detectors, the lighter particles are less likely to transform the initial Landau distribution into Moyal due to reduced interactions with the detector caused by relativistic effects.

5.5 Distinguishability at 105 MeV/c

The COMET project aims to differentiate e^- at approximately 105 MeV/c, the trigger signal for neutrinoless $\mu - e$ conversion, from background signals at approximately 105 MeV/c.

At this energy level, e^- exhibits distinct momentum and energy distributions compared to heavier μ^+ and π^+ particles as they traverse the CTH counters. e^- deposit less energy and consequently experience slower momentum decrease compared to μ^+ and π^+. Although the three particles may initially have similar momentum at CTH 0, their distributions distinctly separate by the time they reach CTH 3, facilitating their differentiation. This makes the CTH detectors effective in distinguishing e^- from μ^+ and π^+ background signals at approximately 105 MeV/c, hence fulfill COMET project's needs.

5.6 Bethe-Bloch Formula

While discrepancies exist, the general trend of energy deposition for e^-, μ^+, and π^+ particles can be accurately predicted by the Bethe-Bloch formula within the momentum range investigated in this project.

A consistent offset is observed for e^- across different momentum levels, potentially attributable to the inclusion of delta-ray path lengths in the primary e^- measurements. Development is needed to refine the algorithm that the analysis software utilises.

The misalignment of π^+ particles may arise from the decay reaction of $\pi^+ \rightarrow \mu^+ + \nu_\mu$. This process has a relatively short mean lifetime, hence is possible to take place as π^+ travels inside the

detector. As momentum increases, particles become more relativistic and hence are less likely to decay, leading to a better alignment with the Bethe-Bloch predictions.

μ^+ particles generally exhibit good alignment with the Bethe-Bloch formula, likely due to their lower likelihood of decay compared to π^+.

5.7 Potential Systematic Errors

The errors associated with the most probable value (MPV) obtained from fitting algorithms may not accurately represent the uncertainties of the fitted values. Alternative methods, such as evaluating the full-width at half-maximum (FWHM) of the histograms, should be considered to analyse uncertainties more comprehensively.

The radiation processes other than atomic collisions, such as Bremsstrahlung radiation and particle decay, are likely to occur in the experimental setup of our concern, therefore should be accounted for when assessing energy deposition behaviours.

The effective atomic number (Z_{eff}) and atomic weight (A_{eff}) derived from the analysis may lack accuracy. Obtaining more precise data from other studies will enhance the accuracy of analysis involving these parameters.

Potential errors in the analysis software for Geant4 simulations, such as the inclusion of delta rays when measuring the path length of e^-, could introduce offsets in the energy deposition values. Further investigation is essential to identify and rectify such discrepancies.

Conclusions

In this project, the response behaviours of Cylindrical Trigger Hodoscope (CTH) detectors upon encountering e^-, μ^+ and π^+ particles at momentum levels of 105, 125, 150 and 200 MeV/c are collected using Geant4-based simulation software. Through analysis of various physical variables, such as impact location, path length, momentum and energy deposition, the particles with lower mass and higher velocity are found to exhibit weaker scattering, lower energy deposition and slower momentum decrease as they travel through the CTH detectors, especially at lower momenta of around 105 MeV/c. This phenomenon enables e^-, which has a significantly smaller mass, to be well distinguished from μ^+ and π^+ at a momentum of around 105 MeV/c. The CTH detector is hence determined to be capable of fulfilling the needs of the COherent Muon to Electron Transition (COMET) project, which aims to detect neutrinoless $\mu - e$ conversions, whose trigger signal is 105 MeV/c e^- radiation, from a huge background, therefore investigate the Beyond Standard Model (BSM) effect of charged-lepton flavour violation (CLFV).

Path length distributions for all three particles consist of a primary peak centred around the expected path length calculated using simulation setup geometry, and a secondary peak that is potentially a result of elastic scattering. Besides, e^- has an extra spike between the primary and secondary peak, which is potentially a result of including the path lengths of secondary delta-rays. This behaviour requires refined algorithm in the analysis software for further investigation.

Moyal distribution provides a good description for the $\Delta E/\Delta x$ readings for all three particles within the investigated range of momenta. For the p readings, despite starting as Landau distributions at CTH counter 0, the distributions increasingly become Moyal as the particles become less relativistic when they travel through subsequent detectors. This aligns with our expectation that the Moyal distribution describes the particle better when the mean number of collisions with the detector is significant.

The fitting results of p and $\Delta E/\Delta x$ readings are compared with the Bethe-Bloch formula results. Despite the overall trend aligns, discrepancies exist between the collected readings and the theoretical predictions, especially for e^- and π^+ particles. The potential systematic uncertainties, such as the effects of delta-ray emission and particle decay, should be investigated in future studies.

Bibliography

[1] R. Abramishvili, G. Adamov, R. R. Akhmetshin, *et al.*, *Comet phase-i technical design report*, Nov. 2020. DOI: 10.1093/ptep/ptz125.

[2] Y. Fujii, *A search for a muon to electron conversion in comet*, Oct. 2023. DOI: 10.1088/1748-0221/18/10/c10010.

[3] Y. Fujii, M. Aoki, S. Dekkers, *et al.*, *Studies of optical fibre and sipm readout system for the cylindrical trigger hodoscope in comet phase-i*.

[4] W. R. L. 1948, *Techniques for nuclear and particle physics experiments : a how-to approach / William R. Leo*, 2nd rev. ed. Tokyo: Springer, 1994, ISBN: 0387572805.

[5] Geant4_Collaboration, *Introduction to geant4*, Dec. 2023.

[6] Y. Fujii, *Cth timing resolution*, Jan. 2024.

[7] L. D. Landau, "On the energy loss of fast particles by ionization," *J. Phys.*, vol. 8, no. 4, pp. 201–205, 1944.

[8] J. E. Moyal, "Xxx. theory of ionization fluctuations," *The London, Edinburgh and Dublin philosophical magazine and journal of science*, vol. 46, no. 374, pp. 263–280, Mar. 1955. DOI: 10.1080/14786440308521076. [Online]. Available: https://www.tandfonline.com/doi/abs/10.1080/14786440308521076.

[9] J. B. Birks, D. W. Fry, L. Costrell, and K. Kandiah, *The Theory and Practice of Scintillation Counting*, 1st ed. Kent: Elsevier Science & Technology, 1964, ISBN: 008010472X. [Online]. Available: https://ebookcentral.proquest.com/lib/[SITE_ID]/detail.action?docID=1828795.

[10] R. C. MURTY, "Effective atomic numbers of heterogeneous materials," *Nature*, vol. 207, no. 4995, pp. 398–399, Jul. 1965. DOI: 10.1038/207398a0. [Online]. Available: http://dx.doi.org/10.1038/207398a0.